Iraqi Journal of Physics, 2024 *Vol. 22, No.4, PP. 21-41*
https://doi.org/10.30723/ijp.v22i4.1318 *P-ISSN: 2070-4003*
E-ISSN: 2664-5548

Nuclear Structure Study Using Relativistic Mean Field (RMF) Method

Sahar M. Aldulaimi[1a*] and Ali A. Alzubadi[1b]
[1]*Department of Physics, College of Science, University of Baghdad, Baghdad, Iraq*
[a*]Corresponding author*: sahar.maged1604a@sc.uobaghdad.edu.iq*
Dr. Ali A. Alzubadi is the chief editor of the journal, but he did not participate in the peer review process other than as an author.

Abstract

The current study uses the relativistic mean field approach to investigate the nuclear structure of selected even-even neutron-rich nuclei spanning from the stability line to the neutron drip line. Specifically, the nuclei studied include $^{16-28}$O, $^{30-42}$Si, $^{48-60}$Ca, $^{56-68}$Ni, $^{88-100}$Kr, $^{96-122}$Ru, $^{140-152}$Ba, $^{142-154}$Sm, and $^{150-162}$Er. The relativistic Hartree-Bogoliubov (RHB) method was applied, incorporating effective density-dependent point coupling (DD-PC) and density-dependent meson exchange (DD-ME) interactions. The impact of these interactions was demonstrated through the calculation of various nuclear structure properties, including binding energy (BE), kinetic energy (KE), pairing energy (PE), root mean square (rms) charge radius, two-neutron separation energy (S_{2n}), mass densities (ρ_m), and triaxial deformation. The calculated results were compared with the available experimental data. It is clear that the RMF approach, particularly with the DD-ME2 and DD-PC1 effective interactions, proved to be a valuable tool for studying nuclear properties near the drip lines and away from stability, providing insights into the behavior of exotic or halo nuclei.

Article Info.

Keywords:
Relativistic Mean Field, Neutron Rich, Meson Exchange, Point Coupling, Even-Even nuclei.

Article history:
Received: Jun. 13, 2024
Revised: Jul. 27,2024
Accepted:Aug. 01, 2024
Published:Dec. 01,2024

I. Introduction

The study of neutron-rich nuclei is a promising area of nuclear structure research that contributes significantly to our knowledge of nuclear physics. However, what happens to nuclei that are far from the stability line is still a mystery. In recent years, there has been a resurgence in interest in nuclear structure models, particularly for heavy-mass range nuclei, as experimental data is only accessible for light nuclei and not abundant. Studying nuclear structural characteristics along the drip lines and away from stability, especially for exotic or halo nuclei located close to the drip lines, relies heavily on theoretical models. Nuclear structure systems are complex, and a solid theoretical model is required to understand the many-body dynamics of nuclei. Although many unstudied stable nuclei form closed systems, it is still possible to study several of them. Our theoretical investigation focused on the nuclear isotopic chain, including ^{28}O, ^{42}Si, ^{60}Ca, ^{80}Ni, ^{100}Kr, ^{122}Ru, ^{152}Ba, ^{154}Sm, and ^{162}Er.

Gangopadhyay has studied the differences between the experimentally and theoretically calculated binding energies in the relativistic mean field (RMF) approach for many odd-Z nuclei ranging from A = 47 to 229 [1]. Marcos et al. [2] calculated the binding energy of two Λ hyperons bound to a nuclear core using the RMF theory. Wang et al. [3] performed RMF calculations systematically for light isotopes (of A < 40) with the non-linear skyrme hartree (NL-SH) parameter set. Additionally, the gap parameter of the bardeen-cooper-schrieffer (BCS) model and the modified Ginzburg-Landau model were used for the first time in the RMF at finite temperatures. Furthermore, Yaghmaei et al. [4] calculated the average binding energy, radii, effective inverse level density parameter, and heat capacity within both methods for even–even isotopes of $^{110-130}$Sn.

The study of nuclei in relativistic and non-relativistic systems can be effectively analyzed using density functional theory (DFT). This theory is the foundation for several models, including the covariant DFT, which has various applications. One such

model, the relativistic Hartree-Bogoliubov (RHB) model, utilizes density-dependent effective interactions of the point-coupling type DD-PC1 and meson exchange DD-ME2 in its calculations. Through numerous tests, the RHB hypothesis has successfully described nuclei near the drip lines and has been used to research unusual deformed nuclides. Other studies based on covariant DFT have also been conducted, focusing on shell structure and shell closure. This theory proves to be a useful tool for studying many-body systems with important ground-state parameters, such as binding energy (BE), kinetic energy (KE), pairing energy (PE), root mean square (rms) radius, two-neutron separation energy (S_{2n}), mass density (ρ_m) and triaxial deformation.

The current study is divided into four sections. Section 2 gives a brief summary of the theoretical formalism of the RHB model. Section 3 presents and analyzes the calculated results. Lastly, section 4 provides a summary of the analysis's findings and conclusions.

2. Theoretical Part

2.1. Mean Field Theory

In nuclear physics, the many-body system issue can be effectively solved with the help of the mean field (MF) theory. Since the many-body Schrödinger equation cannot be solved to obtain a good approximation of a highly interacting system, one solution is to transform the system so that it is made up of quasi-particles with other interactions. The perturbation theory can handle any remaining interactions [5]. In this case, the Hamiltonian system is [6]:

$$\hat{H} = \hat{T} + \hat{V} = \sum_{i=1}^{A} t(r_i) + \sum_{\substack{i,j=1 \\ i<j}}^{A} v(r_i, r_j) = \sum_{i=1}^{A} \frac{-\hbar^2}{2m_N} {\nabla_i}^2 + \sum_{\substack{i,j=1 \\ i<j}}^{A} v(r_i, r_j) \qquad (\mathbf{1})$$

where m_N denotes the nucleon mass, r_i denotes the *i*-coordinates, T represents the kinetic energies, and V represents the potential energies. The nuclear MF has to be derived from a process that is roughly similar to the Hartree-Fock (HF) one. Skyrme's density-dependent nucleon-nucleon interaction formula is implemented in the MF theory, making it optimal for closed-shell nuclei. The results for BE, density, and single-particle energies near the Fermi level are excellent when this method is used [7]. The influential interaction forces are directly parametrized in the HF method. The Skyrme Hartree-Fock (SHF) interaction [8], is one of the forces we considered. RMF theory [9], a classical relativistic theory of fields, is another key tool for studying the nuclear many-body system. According to this model, nucleons have a four-part wave function ψ_i like Dirac quantum mechanical particles. As they travel through many classical meson fields, the motion of these particles is dynamically relativistic. The MF technique is based primarily on using Dirac's four-spinor wave functions in the RMF framework for a solitary nucleon and the non-relativistic SHF [10, 11] procedure to produce a two-component-spinor wave function.

2.2. Hartree-Fock Theory

The HF approximation depends on fermions' compliance with the Pauli exclusion principle; therefore, it is easy to characterize how a nucleus exerts its force by considering how each nucleon acts when floating freely in a mean potential. This is one of the test wavefunctions that might help to understand the HF approximation. Here, a Slater determinant stands for A-nucleon ground states. Since, at first, only the precise spatial forms of the wave function for a single particle are known, the wave function of

an oscillator might be utilized to address this issue [8]. For an A-particle system, the HF approximation [12] makes it possible to express the entire Hamiltonian in terms of two forces acting on the particles and one component of kinetic energy

$$\widehat{\mathcal{H}} = \sum_{i=1}^{A} \frac{\hat{p}^2}{2m_i} + \frac{1}{2}\sum_{i\neq j}^{A} V(r_i, r_j), \qquad (2)$$

where $V(r_i,r_j)$ includes the Coulomb interaction and all the other forces involved in a nucleon-nucleon contact. By comparing the total Hamiltonian's expected value to the HF wave function, one can attempt to describe the ground-state energy

$$E_{HF}^{0} = \langle \psi_{HF} | \widehat{\mathcal{H}} | \psi_{HF} \rangle$$
$$= \frac{-\hbar^2}{2m}\sum_{i=1}^{A}\int \psi_i{}^{*}(r)\nabla^2\psi_i(r) + \frac{1}{2}\sum_{i\neq j}^{A}\int\int \psi_i^{*}(r)\psi_j^{*}(r')V(r,r')\psi_i(r)\psi_j(r')drdr'$$
$$-\frac{1}{2}\sum_{i\neq j}^{A}\int\int \psi_i^{*}(r)\psi_j^{*}(r')V(r,r')\psi_i(r')\psi_j(r)drdr' \qquad (3)$$

2.3. Relativistic Approximation

Combining RMF theory with the relativistic Hartree (RH) method and the no-sea approximation has successfully been used to investigate some nuclear processes. Despite RMF naturally integrating the spin-orbit interaction, the concern is that RMF needs to consider other effective spin-orbit interactions like the nuclear tensor force. Recently, the density-dependence relativistic Hartree-Fock (DDRHF) RMF approach has been proposed for nuclear structures [13]. Using this idea in the relativistic Hartree-Fock Bogoliubov (RHFB) theory [14], exotic, unstable nuclei could be investigated. The Bogoliubov scheme, which enables efficient control of the continuum effect, is made possible by RHFB integration of the MF and the pairing field.

Relativistic energy density functional (EDF) [15] characterizes the ground state and collective excitation of nuclei uniformly and globally over the entire nuclide table [16], which is why nuclear structure research heavily relies on them. Utilizing the single-particle Hamiltonian *h* and the Dirac equation along with the energy deflection function (EDF), where the latter is derived from the energy functional E[ρ] [17], DFT develops the fundamental idea of relativistic approximation. To exchange mesons like Isoscalar-scalar mesons, Isoscalar-vector mesons, and Z bosons, standard quantum hydrodynamics (QHD) depicts the nucleus as a system of Dirac nucleons connected by an efficient Lagrangian [13]. The only kind of meson fields that may be used is isovector-vector fields. Currently, covariant density functional (CDF) theory [18] is the most advanced theoretical framework. There are three types of CDF models: the density-dependence meson-exchange model (DD-ME) [19], the density-dependence point coupling (DD-PC) [20] and the non-linear meson-nucleon coupling model (NL) [21]. The coupling structure between the DD-ME and DD-PC models consists of two vector terms and an Isoscalar-scalar term [22]. The ground state properties of neutron-rich nuclei are examined in this study using both the finite-range interaction DD-ME and the zero-range interaction DD-PC.

2.3.1. Density Dependency Model for Meson Exchange

Since mesons are not quantized, Fock terms are superfluous, and all they do is introduce relativistic accurate classical fields into the nucleus, which is their only purpose. Using the quantum numbers and the CDF framework, the Lagrangian density of this model may be determined without taking into account the effects of the Dirac Sea (the "no-sea approximation"). Theorize as defined by [5]

$$\mathcal{L} = \mathcal{L}_{\mathrm{N}} + \mathcal{L}_{\mathrm{m}} + \mathcal{L}_{\mathrm{int}}. \tag{4}$$

Free nucleons ($\mathcal{L}_N$) have the following Lagrangian

$$\mathcal{L}_{\mathrm{N}} = \bar{\psi}\left(\mathrm{i}\gamma_{\mu}\,\partial^{\mu} - \mathrm{m}\right)\psi, \tag{5}$$

where ψ is the Dirac spinor and m is the atomic mass. To indicate the Lagrangian of the electromagnetic field and the free meson fields, $\mathcal{L}_{\mathrm{m}}$ is

$$\mathcal{L}_{\mathrm{m}} = \frac{1}{2}\partial_{\mu}\sigma\,\partial^{\mu}\sigma - \frac{1}{2}\mathrm{m}_{\sigma}^{2}\sigma^{2} - \frac{1}{2}\Omega_{\mu\mathrm{v}}\Omega^{\mu\mathrm{v}} + \frac{1}{2}\mathrm{m}_{\omega}^{2}\omega_{\mu}\omega^{\mu} - \frac{1}{4}\mathrm{R}_{\mu\mathrm{v}}\,.\,\mathrm{R}^{\mu\mathrm{v}} + \frac{1}{2}\mathrm{m}_{\rho}^{2}\rho_{\mu}\,.\,\rho^{\mu} - \frac{1}{4}\mathrm{F}_{\mu\mathrm{v}}\,.\,\mathrm{F}^{\mu\mathrm{v}} \tag{6}$$

Where $\Omega_{\mu v}$, $R_{\mu V}$, and $F_{\mu v}$ are the field tensors and m_{σ}, m_{ω} and m_{ρ} are the corresponding masses.

$$\mathrm{R}_{\mu\mathrm{v}} = \partial_{\mu}\rho_{\mathrm{v}} - \partial_{\mathrm{v}}\rho_{\mu}\ , \quad \Omega_{\mu\mathrm{v}} = \partial_{\mu}\omega_{\mathrm{v}} - \partial_{\mathrm{v}}\omega_{\mu}\ , \qquad \mathrm{F}_{\mu\mathrm{v}} = \partial_{\mu}\mathrm{A}_{\mathrm{v}} - \partial_{\mathrm{v}}\mathrm{A}_{\mu} \tag{7}$$

In contrast to the italicized letters used to symbolize vectors in regular space, arrows were employed to depict motion in isovector space. $\mathcal{L}_{int}$ contains the bare minimum of interaction words.

$$\mathcal{L}_{\mathrm{int}} = -\mathrm{g}_{\sigma}\bar{\psi}\psi\sigma - \mathrm{g}_{\omega}\bar{\psi}\gamma^{\mu}\psi\omega_{\mu} - \mathrm{g}_{\rho}\bar{\psi}\tau\gamma^{\mu}\psi.\,\rho_{\mu} - \mathrm{e}\bar{\psi}\gamma^{\mu}\psi\mathrm{A}_{\mu} \tag{8}$$

The g_{σ}, g_{ω}, g_{ρ}, and *e* are the coupling constants, and τ is the Pauli isospin matrices.

Through using the g_{σ}, g_{ρ} ,g_{ω}, and e-connections, the nuclear matter and its underlying ground state are simulated using these constants and the unknown meson masses. In this model, the isoscalar-scalar meson supplies attractive nuclear interaction at intermediate and long ranges. In contrast, the repulsive component of the interaction at shorter ranges is provided by the isoscalar-vector meson [19]. Bilinear forms on the Lorentz scalar are postulated at the vertices of the coupling constants [23]. Operators on atomic nuclei are often functions of the vector density in practical contexts [24].

$$\rho_{\mathrm{v}} = \sqrt{\mathrm{j}_{\mu}\mathrm{j}^{\mu}}, \ \text{ with } \mathrm{j}_{\mu} = \bar{\psi}\gamma_{\mu}\psi\,. \tag{9}$$

In the static scenario, the Hamiltonian density may be calculated directly from the Lagrangian density using the formula given by Yaghmaei et al. [4]

$$\mathcal{H}(\mathrm{r}) = \sum_{\mathrm{i}}^{\mathrm{A}} \psi_{\mathrm{i}}^{\dagger}\,(\alpha \mathrm{p} + \beta \mathrm{m})\psi_{\mathrm{i}} + \frac{1}{2}[(\nabla\sigma)^2 + \mathrm{m}_{\sigma}^2] - \frac{1}{2}[(\nabla\omega)^2 + \mathrm{m}_{\omega}^2\omega^2] - \frac{1}{2}\left[(\nabla\rho)^2 + \mathrm{m}_{\rho}^2\rho^2\right] - \frac{1}{2}(\nabla \mathrm{A})^2 + \left[\mathrm{g}_{\sigma}\rho_{\mathrm{S}}\sigma + \mathrm{g}_{\omega}\mathrm{j}_{\mu}\omega^{\mu} + \mathrm{g}_{\rho}\mathrm{j}_{\mu}\,.\,\rho^{\mu} + \mathrm{e}\mathrm{j}_{\mathrm{p}\mu}\mathrm{A}^{\mu}\right]. \quad (\mathbf{10})$$

where H(r) is the Hamiltonian that depends on the position r and represents the total energy of the system, A is the vector potential associated with the magnetic interaction, $\psi_{\mathrm{i}}^{\dagger}$ is the adjoint transition matrix for state i, α, β are Dirac matrices, p is the momentum related to motion, m is the rest mass of the particle, ∇ is the gradient operator, σ is the scalar field of the nucleus ,ω is the vector field of the nucleus, ρ is the vector field of the nucleus, S is the nuclear spin, $\mathrm{g}_{\sigma}, \mathrm{g}_{\omega}, \mathrm{g}_{\rho}$ are the coupling constants for interactions between fields, j_{μ} is the current density, e is the electric charge, and A^{μ} is the spatial components of the vector potential.

The RHFB model's most effective EDF is a particle-based one. The self-consistency of both the particle-hole (p-h) and particle-particle (p-p) channels is maintained. The CDF energy density of the RHFB model is determined by the Hamiltonian H of the system and its projected value concerning the wave function in the ground state |Φ⟩:

$$\mathrm{E} = \langle\Phi|\mathcal{H}|\Phi\rangle \quad (\mathbf{11})$$

To calculate the RHB EDF, we adjusted the energy functional in Eq. (11) based on the Dirac spinor ψ(r)

$$\mathrm{E}_{\mathrm{RHB}}[\rho, \mathrm{k}] = \mathrm{E}_{\mathrm{RMF}}[\rho] + \mathrm{E}_{\mathrm{pair}}[\mathrm{k}], \quad (\mathbf{12})$$

The RMF energy functional, designated by $E_{RMF}[\rho]$, is obtained by integrating the Hamiltonian Eq. (10) across the r-space

$$\mathrm{E}_{\mathrm{RMF}}[\rho] = \int \mathrm{d}^3\,\mathrm{r}\mathrm{H}(\mathrm{r}) \quad (\mathbf{13})$$

Cooper pair scattering to the continuum through the pairing interaction is enabled by the nucleon separation energy, denoted by the $\mathrm{E}_{\mathrm{pair}}[\mathrm{k}]$ pairing component, which is comparable to the pairing gap energy. To extract this energy, we must first solve the RHB energy function [13]

$$\mathrm{E}_{\mathrm{pair}}[\mathrm{k}] = \frac{1}{4}\sum_{\mathrm{n}_1\mathrm{n}_1,}\sum_{\mathrm{n}_2\mathrm{n}_2,} \mathrm{k}^{*}_{\mathrm{n}_1\mathrm{n}_1}, \langle \mathrm{n}_1\mathrm{n}_1\,'|\mathrm{V}^{\mathrm{PP}}|\mathrm{n}_2\mathrm{n}_2\,'\rangle\, \mathrm{k}_{\mathrm{n}_2\mathrm{n}_2}\,' \quad (\mathbf{14})$$

which satisfies $\langle n_1 n_1\,'|V^{PP}|n_2 n_2\,'\rangle$ may be considered the density matrix and pairing tensor for a single body, respectively, and represent the pairing interaction between two bodies, respectively. The RHB equation may be derived using the theory of variations as shown [21]

$$\begin{pmatrix} h_D - \lambda & \Delta \\ -\Delta^* & -(h_D + \lambda)^* \end{pmatrix} = E \begin{pmatrix} U \\ V \end{pmatrix} \quad (\mathbf{15})$$

where h_D denotes the m mass Dirac nucleon Hamiltonian. The chemical potential λ is described in terms of neutron and proton average particle number restrictions. Here, V and U are the Dirac spinors (energy quantifiers) of the quasi-particles, and E is the energy of the quasi-particles. The Dirac Hamiltonian, often known as

$$\hat{h}_D = \alpha(p - \Sigma) + \Sigma_0 + \beta(M + \Sigma_s) \quad (\mathbf{16})$$

The attractive scalar potential is represented as follows in terms of the nucleon's self-energies Σ_s

$$\Sigma_s(r) = g_\sigma \sigma(r) \quad (\mathbf{17})$$

The term $\Sigma s(r)$ denotes the scalar potential at a specific position r within the nucleus, $g\sigma$ represents the coupling constant associated with the scalar field interaction in the nuclear model, and $\sigma(r)$ corresponds to the scalar field distribution within the nucleus. For the repulsive vector potential

$$\Sigma_0(r) = g_\omega \omega_0(r) + g_\rho \tau . \rho_0(r) + eA_0(r) + \Sigma_0^R(r) \quad (\mathbf{18})$$

This component includes terms involving the omega field ($\omega_0(r)$), the rho field ($\tau \cdot \rho_0(r)$), the vector potential ($A_0(r)$), and a residual component Σ_0^R(r).
The magnetic potential is:

$$\Sigma_\mu = g_\omega \omega_\mu(r) + g_\rho \tau . \rho_\mu(r) + eA_\mu(r) + \Sigma_\mu^R(r) \quad (\mathbf{19})$$

where Σ_μ is the total current density, $g_\omega$is the coupling constant associated with the ω field, $\omega_\mu(r)$is the vector field ω at position r, g_ρ is the coupling constant associated with the ρ field, τ is the isospin operator, $\rho_\mu(r)$ is the vector field ρ at position r, e is the electric charge, $A_\mu(r)$ is the vector potential A at position r, and $\Sigma_\mu^R(r)$ is the external current density.

2.3.2. Point-Coupling Models with Density Dependence

Point-coupling models may be considered as a special case of the RMF framework that satisfies the principle of internal consistency. In complete identification to the ME phenomenology [13], where the smallest set of meson fields necessary for a quantitative description of the nucleus consists of the Isoscalar-scalar meson, the isovector-vector meson, and the isovector-vector meson. Similar local interactions [20] between nucleons have been created as a replacement for these pathways, with density dependence coming either from the two-body coupling constant contacts or the contact of many-body potential conditions [13].

The effective Lagrangian includes the interactions of the isoscalar, isovectors, and scalars for a total of four fermions. For which the textual form is [25]

$$\mathcal{L} = \bar{\psi}(\mathrm{i}\gamma.\partial - \mathrm{m})\psi - \frac{1}{2}\alpha_S(\hat{\rho})(\bar{\psi}\psi)(\bar{\psi}\psi) - \frac{1}{2}\alpha_V(\hat{\rho})(\bar{\psi}\gamma^\mu\psi)\left(\bar{\psi}\gamma_\mu\psi\right) - \frac{1}{2}\alpha_{TV}(\hat{\rho})(\bar{\psi}\tau\gamma^\mu\psi)\left(\bar{\psi}\tau\gamma_\mu\psi\right) - \frac{1}{2}\delta_S(\partial_\nu\bar{\psi}\psi)(\partial^\nu\bar{\psi}\mu\psi) - \mathrm{e}\bar{\psi}\gamma\mathrm{A}\frac{1-\tau_3}{2}\psi \quad (\mathbf{20})$$

The free-nucleon Lagrangian and point-coupling interaction components are also included in the model, along with the coupling of protons to the electromagnetic field. Quantitatively characterizing the nuclear density distribution (in terms of nuclear radii) relies on a precise understanding of the effects of finite-range interactions, which were described by the derivative term in Eq. (20). In each space-isospace channel, similar interactions can be involved but only constrain a single derivative term in particle data involved, for example $\delta_S(\partial_\nu\bar{\psi}\psi)(\partial^\nu\bar{\psi}\psi)$. The acceptable derivative term only consistently appears in the isoscalar-scalar channel and traditional meson-exchange RMF models, where the mass of the meson is viewed as a free parameter, even though the masses of the mesons are set at random. By coupling constants in Eq. (20), the interaction terms can be understood as functionals of the nucleon four-current

$$\mathrm{j}^\mu = \bar{\psi}\gamma^\mu\psi = \hat{\rho}\mathrm{u}^\mu \quad (\mathbf{21})$$

where u^μ is a 4-velocity expressed as $(1-\mathrm{v}^2)^{1/2}(1,\mathrm{v})$.

The nuclear matter is homogeneous, so its rest frame velocity is 0. The Hamiltonian density $\mathcal{H}(\mathrm{r})$and EDF for the point-coupling model are derived using a Lagrangian density and the Euler-Lagrange Equation [4][9]

$$E_{RMF}[\psi,\bar{\psi},A_\mu] = \int d^3rH(r) = \sum_{i=1}^{A}\int d^3r\psi_i^\dagger(\alpha\mathrm{p}+\beta m)\psi_i - \frac{1}{2}(\nabla A)^2 + \frac{1}{2}e\int d^3\,rj_p^\mu A_\mu + \frac{1}{2}\int d^3\,r\left[\alpha_S\rho_S^2 + \alpha_V j_\mu j^\mu + \alpha_{TV}j_\mu.j^\mu + \delta_S\rho_S\rho_S\right] \quad (\mathbf{22})$$

From the derivative of the EDF concerning the Dirac spinors ψ in Eq. (22)

$$\{-\mathrm{i}\alpha\nabla + \beta\mathrm{M}^*(\mathrm{r}) + \mathrm{V}(\mathrm{r})\}\psi_\mathrm{i}(\mathrm{r}) = \epsilon_\mathrm{i}\psi_\mathrm{i}(\mathrm{r}) \quad (\mathbf{23})$$

under the assumption that time-reversal invariance can be verified. To define the Dirac effective mass, we need

$$\mathrm{M}^* = \mathrm{m} + \Sigma_\mathrm{s} = \mathrm{m} + \delta_\mathrm{S}\rho_\mathrm{S} + \delta_\mathrm{S}\Delta\rho_\mathrm{S} \quad (\mathbf{24})$$

whereas the definition of the vector potential is:

$$\mathrm{V}(\mathrm{r}) = \alpha_\mathrm{V}\rho_\mathrm{v} + \alpha_\mathrm{TV}\tau_3\rho_\mathrm{tv} + \mathrm{eA}_0 + \Sigma_0^\mathrm{R} \quad (\mathbf{25})$$

The rearrangement contribution, indicated by Σ_0^R, is a function of the variation of the couplings α_S , α_V , and α_{TV}. According to the nucleon fields in the density operator

$$\Sigma_0^{\mathrm{R}} = \frac{\partial \alpha_{\mathrm{S}}}{\partial \rho_{\mathrm{v}}} \rho_{\mathrm{s}}^2 + \frac{\partial \alpha_{\mathrm{V}}}{\partial \rho_{\mathrm{v}}} \rho_{\mathrm{v}}^2 + \frac{\partial \alpha_{\mathrm{TV}}}{\partial \rho_{\mathrm{v}}} \rho_{\mathrm{tv}}^2 \qquad (\mathbf{26})$$

The rearrangement of self-energy must be taken into consideration [24] to ensure that the model is thermodynamically and kinematically consistent and that energy and momentum are conserved.

3. Results and Discussions

In this investigation, a thorough analysis was conducted on the nuclear properties of specific isotope chains, including $^{16\text{-}28}$O, $^{30\text{-}42}$Si, $^{48\text{-}60}$Ca, $^{56\text{-}68}$Ni, $^{88\text{-}100}$Kr, $^{96\text{-}122}$Ru, $^{140\text{-}152}$Ba, $^{142\text{-}152}$Sm, and $^{150\text{-}162}$Er. The results were calculated using RMF and then compared with available experimental data. As depicted in Fig. 1, the ground-state binding energies were calculated using both DD-ME2 and DD-PC1 effective interactions and compared with experimental data from the National Nuclear Data Center [26]. The binding energy (BE) increased with the rise in mass number. Our results are in good agreement with the general trend of the experimental data, with the exception of Kr and Ba isotopes. In both cases, our calculations underestimated the experimental data for both parameterizations. As illustrated in Figure 2, the kinetic energy (KE) also increased with the rise in mass number. Notably, a significant concordance is observed between ME2 and PC1 in isotopes $^{16\text{-}28}$O and $^{30\text{-}42}$Si, while a minor disparity in KE values is noted between ME2 and PC1 of the isotopes $^{48\text{-}60}$Ca, $^{56\text{-}68}$Ni, $^{88\text{-}100}$Kr, $^{96\text{-}120}$Ru, $^{140\text{-}152}$Ba, $^{142\text{-}154}$Sm, and $^{150\text{-}162}$Er. The difference in kinetic energy values between ME2 and PC1 model may be due to different theoretical structures; underlying assumptions in the two models functionally dependent droplet- like interactions between the interfaces can lead to differences in the predicted kinetic energy values, especially for isotopes with a certain number of atoms that may contain meson exchange or point-join interactions.

The pairing energy is a fundamental aspect of nuclear structure, representing the energy associated with pairing nucleons in a nucleus. In the context of neutron-rich nuclei, the behavior of the pairing energy curve can offer valuable insights into the nuclear properties and stability of these exotic systems. The pairing energy curve typically demonstrates distinctive trends as the number of neutrons increases within a nucleus and strong agreement between the ME2 and PC1 interactions for most isotopes. Various factors influence its behavior, such as the neutron shell structure, the occupation of neutron energy levels, and the interplay of nuclear forces within the nucleus. The pairing energy trend observed in the nuclei in Fig. 3 follows a consistent pattern across different isotopes, reflecting the interplay between nuclear structure and neutron numbers. For $^{16\text{-}28}$O isotopes, the pairing energy values decreased as the neutron number approached the magic numbers, resulting in lower pairing energies due to the formation of closed-shell configurations. The pairing energy curve for $^{30\text{-}42}$Si isotopes showed a non-linear trend and abrupt changes in the pairing energy values. This is due to the influence of shell structure evolution, magic numbers, and the onset of deformation on the pairing energy variations in silicon isotopes. The pairing energy curves for Ca, Ni, Kr, Ba and Er isotopes showed consistent trends as the number of neutrons increased within the isotopic chains. The behavior of the pairing energy curves is influenced by factors such as the neutron shell structure, the occupation of neutron energy levels, and the interplay of nuclear forces within the nucleus. In the case of Ru isotopes, there was a noticeable gradual increase in the discrepancy in pairing energy

calculations for isotopes ^{112}Ru, ^{114}Ru, and ^{116}Ru when using the ME2 and PC1 interactions. These differences are influenced by the changing neutron numbers, sensitivity to neutron interactions, and the treatment of pairing factors, all of which collectively contribute to the growing disparity in the pairing energy results as the neutron number varies across the isotopes. The pairing energy curve for Sm isotopes showed a rapid decrease, especially for the ^{144}Sm isotope with N=82, compared to other Sm isotopes. This is due to strong pairing correlations resulting from the presence of a magic number, causing a more significant pairing effect than in other Sm isotopes. This behavior results in a considerable reduction in the energy associated with pairing nucleons, indicating the strong binding and stability of the nucleus.

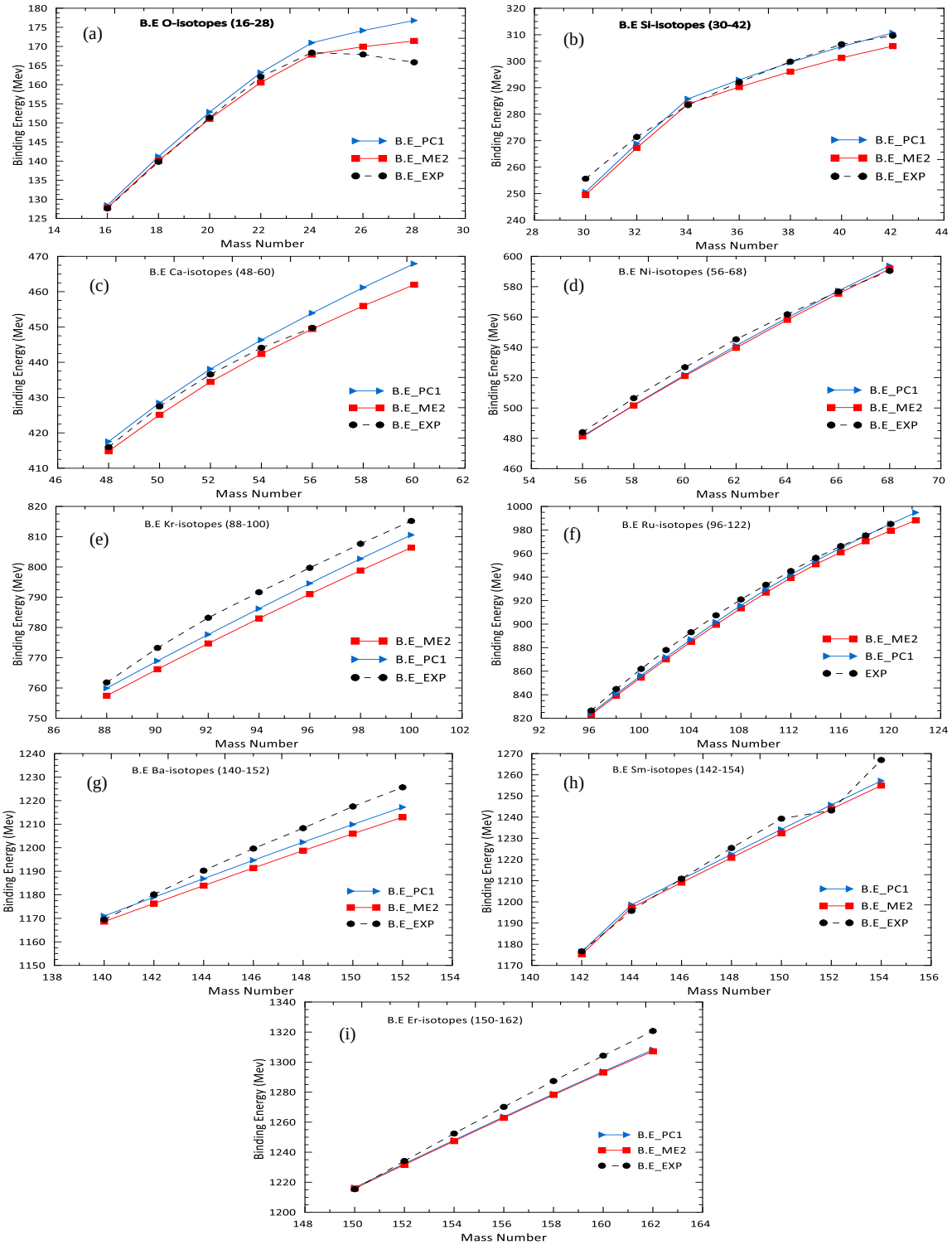

Figure 1: The binding energy (BE) in MeV as a function of mass number (A) for even-even: (a) $^{16–28}$O, (b) $^{30–42}$Si, (c) $^{48–60}$Ca, (d) $^{56–68}$Ni, (e) $^{88–100}$Kr, (f) $^{96–122}$Ru, (g) $^{140–152}$Ba, (h) $^{142–154}$Sm and (i) $^{150–162}$Er isotopes, using ME2, PC1 interactions. In comparison with the experimental data of the National Nuclear Data Center [25].

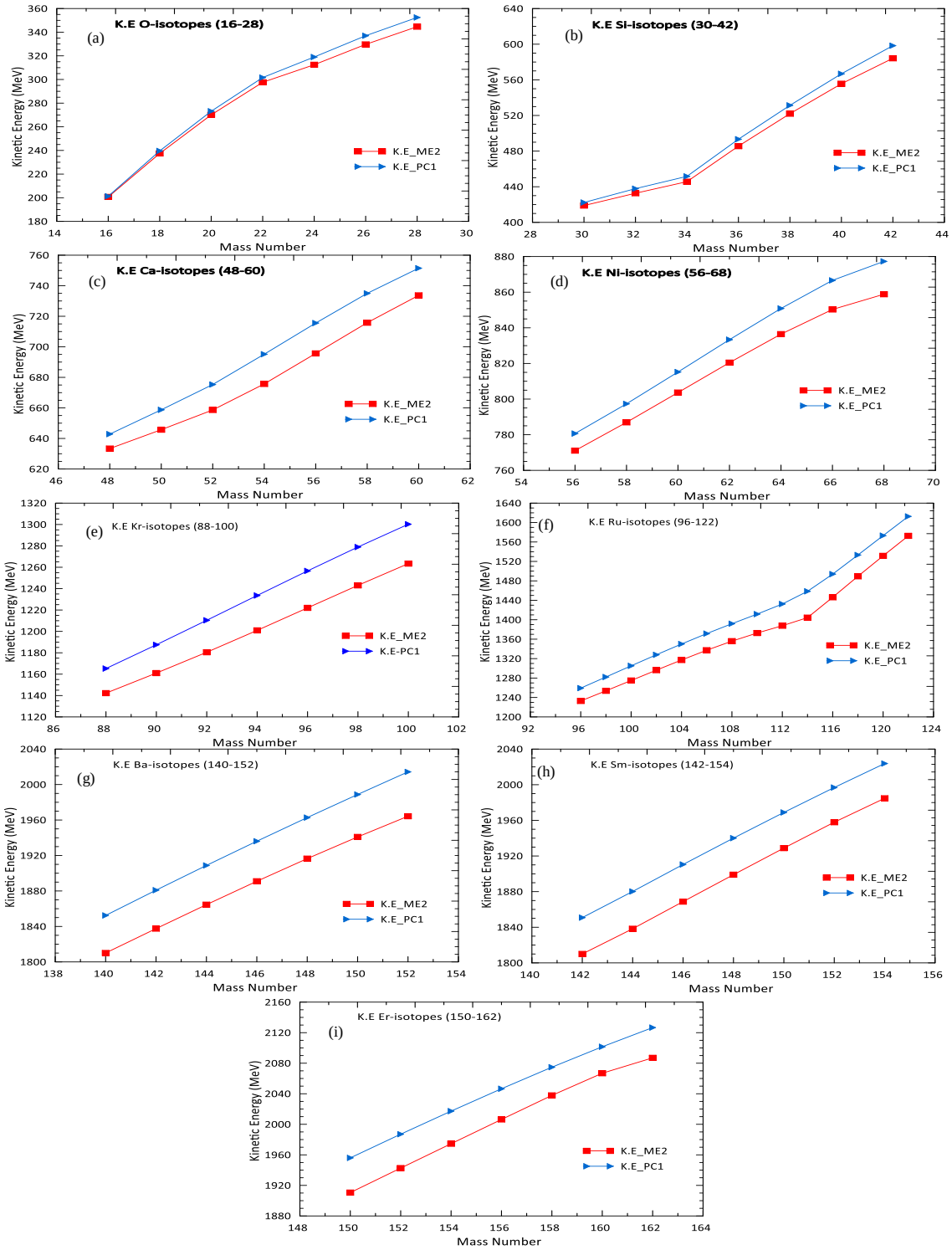

Figure 2: The kinetic energy (KE) in MeV as a function of mass number (A) for even-even: (a) $^{16–28}$O, (b) $^{30–42}$Si, (c) $^{48–60}$Ca, (d) $^{56–68}$Ni, (e) $^{88–100}$Kr, (f) $^{96–122}$Ru, (g) $^{140–152}$Ba, (h) $^{142–154}$Sm and (i) $^{150–162}$Er isotopes, using ME2, PC1 interactions.

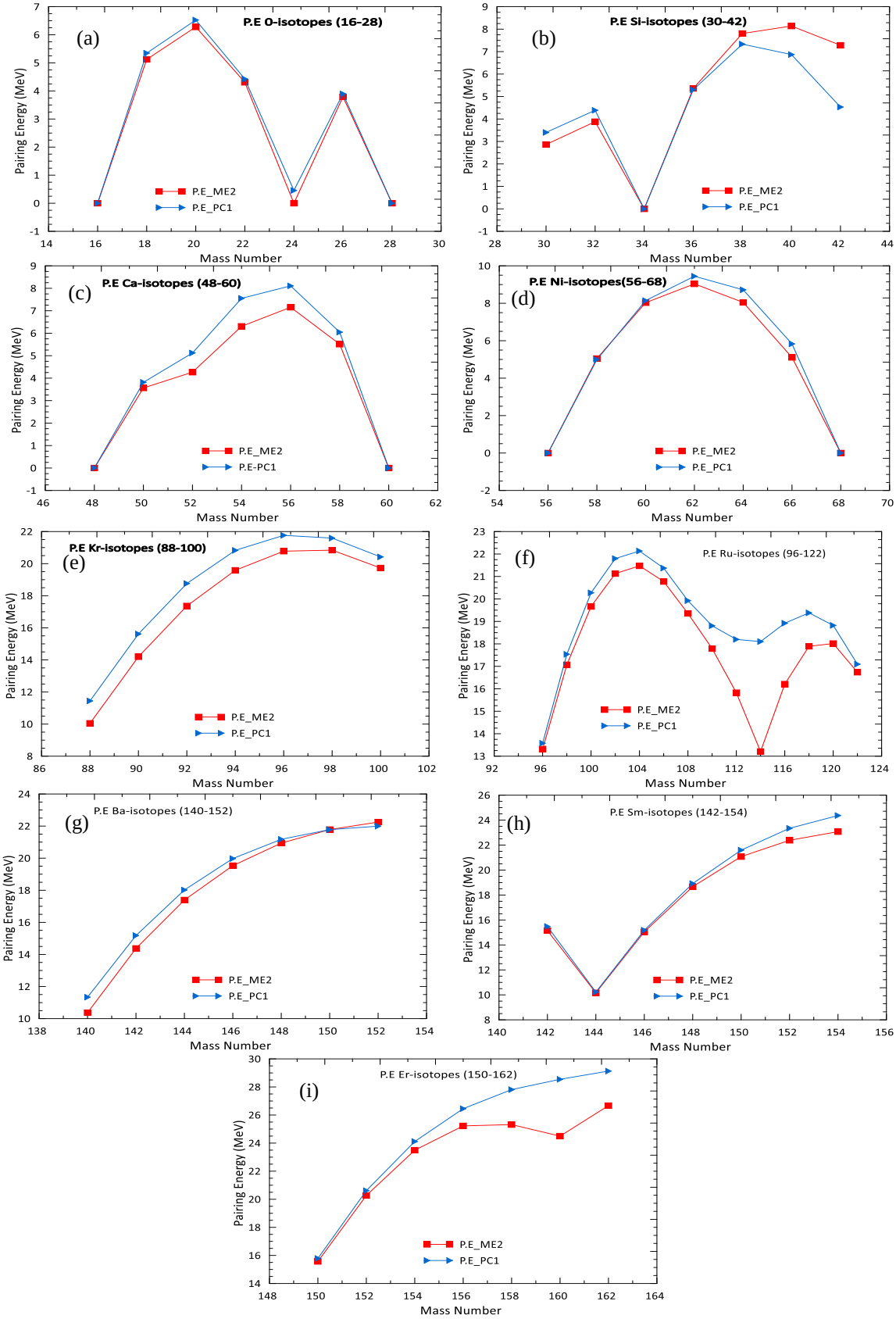

Figure 3: The pairing energy (PE) in MeV as a function of mass number (A) for even-even: (a) $^{16–28}$O, (b) $^{30–42}$Si, (c) $^{48–60}$Ca, (d) $^{56–68}$Ni, (e) $^{88–100}$Kr, (f) $^{96–122}$Ru, (g) $^{140–152}$Ba, (h) $^{142–154}$Sm and (i) $^{150–162}$Er isotopes, using ME2, PC1 interactions.

Fig. 4 illustrates the calculated rms charge radii of each isotopic chain, which exhibit systematic trends as the number of neutrons increases within the nucleus. With the addition of neutrons, the nuclear size may change due to the influence of the neutron distribution on the overall charge distribution of the nucleus. The behavior of rms charge radii for isotopic chains can be understood in terms of systematic trends with neutron number, the influence of magic numbers and shell effects, nuclear deformation and shape changes, and the impact of pairing effects on nuclear stability and charge distribution. These physical interpretations provide insights into the variations observed in the rms charge radii for different isotopes within the isotopic chains studied in the paper. Comparison with experimental data for each isotopic chain, as shown in Fig. 4, showed a reasonable agreement in rms charge radii [27]. This suggests that the model used in the study effectively predicts the charge distribution and nuclear properties of the isotopes studied. The good alignment between experimental and theoretical results validates the model's capability to accurately describe these isotopes' nuclear structure. The differences in the calculated rms charge radius curves using the PC1 and ME2 interactions, especially in Ni isotopes, can be attributed to the distinct characteristics, assumptions, parameterizations, and treatment of nuclear structure effects within the theoretical model. These discrepancies highlight the importance of understanding the nuances of different effective interactions and their impact on predicting nuclear properties accurately.

The discrepancies between the PC1 and ME2 interactions result in calculating the rms charge radii for nickel isotopes (Z=28) while showing good agreement in oxygen (Z=8) and calcium (Z=20) isotopes with the proton magic numbers attributed to the unique combination of nuclear symmetry effects, shell structure properties, deformation characteristics, and sensitivity to effective interaction parameters specific to nickel isotopes. These factors highlight the intricate nature of nuclear structure modeling and the need to consider the nuanced behavior of isotopes with different proton numbers in theoretical calculations.

Fig. 5 shows the calculated two-neutron separation energy (S_{2n}) for each isotopic chain. This energy is crucial for understanding nuclear stability, shell structure effects, nuclear interactions, predicting nuclear reactions, studying nuclear structure evolution, and exploring exotic nuclei near the drip lines. It is a fundamental quantity in nuclear physics research and significantly contributes to our understanding of the properties and behavior of atomic nuclei. In the case of oxygen isotopes, a sudden shift in slope was observed for certain isotopes, such as ^{26}O, due to a closed shell structure. This suggests a significant energy barrier for removing two neutrons, resulting from the stability conferred by the magic number of neutrons. The difference between experimental and theoretical S_{2n} values for specific isotopes may indicate the influence of shell closures and the need for a more refined theoretical description of these nuclei. A discrepancy appeared between theoretical predictions and experimental S_{2n} values for Si isotopes, which may indicate limitations in the theoretical approach used. The behavior of S_{2n} in Ca isotopes showed slight differences between experimental and theoretical S_{2n} values for certain isotopes ($^{50,\ 56}$Ca). This may suggest variations in the nuclear structure properties and the impact of the effective interactions used in the calculations. The presence of magic numbers in calcium isotopes can lead to specific trends in the S_{2n} values, indicating the stability of these isotopes against neutron removal. For Ni isotopes, the behavior of S_{2n} can reveal a sudden shift in slope observed for certain Ni isotopes ($^{58,\ 64,\ 66,\ 68}$Ni), which may indicate the presence of closed shell structures and the associated energy barriers for neutron separation.

The S_{2n} curve for Kr isotopes using the PC1 interaction showed a particular trend in the separation energies, indicating the stability of these isotopes against neutron

removal. The ME2 interaction exhibited a slightly different trend compared to PC1, potentially reflecting variations in the nuclear structure properties and effective interactions. The discrepancies between the theoretical predictions using PC1 and ME2 interactions and the experimental data may suggest limitations in the theoretical approach used or the need for a more refined description of these nuclei. The S_{2n} curve for Ru isotopes with the PC1 interaction showed a gradual increase or decrease in separation energies, influenced by the varying neutron numbers and pairing effects. When using the ME2 interaction, the S_{2n} curve aligned with the PC1 curve, and both were in good agreement with experimental data.

The (S_{2n}) curve for Ba, Sm, and Er isotopes with the PC1 and ME2 interactions demonstrated a clear and consistent pattern, adhering to the expected behavior. However, a noticeable discrepancy arised when comparing these curves to the experimental data. Nonetheless, the overall trend of the separation energy changing alongside the increasing number of neutrons remained consistent with theoretical expectations. The discrepancies between the calculated S_{2n} values and the experimental data could indicate areas where the models may need adjustments or refinements.

The mass density distribution and triaxial deformation shown in Fig. 6 are for selected isotopes with the highest mass number from the investigated isotopic chains and close to the neutron drip line, specifically, ^{28}O, ^{42}Si, ^{58}Ca, ^{68}Ni, ^{100}Kr, ^{122}Ru, ^{152}Ba, ^{154}Sm, and ^{162}Er.

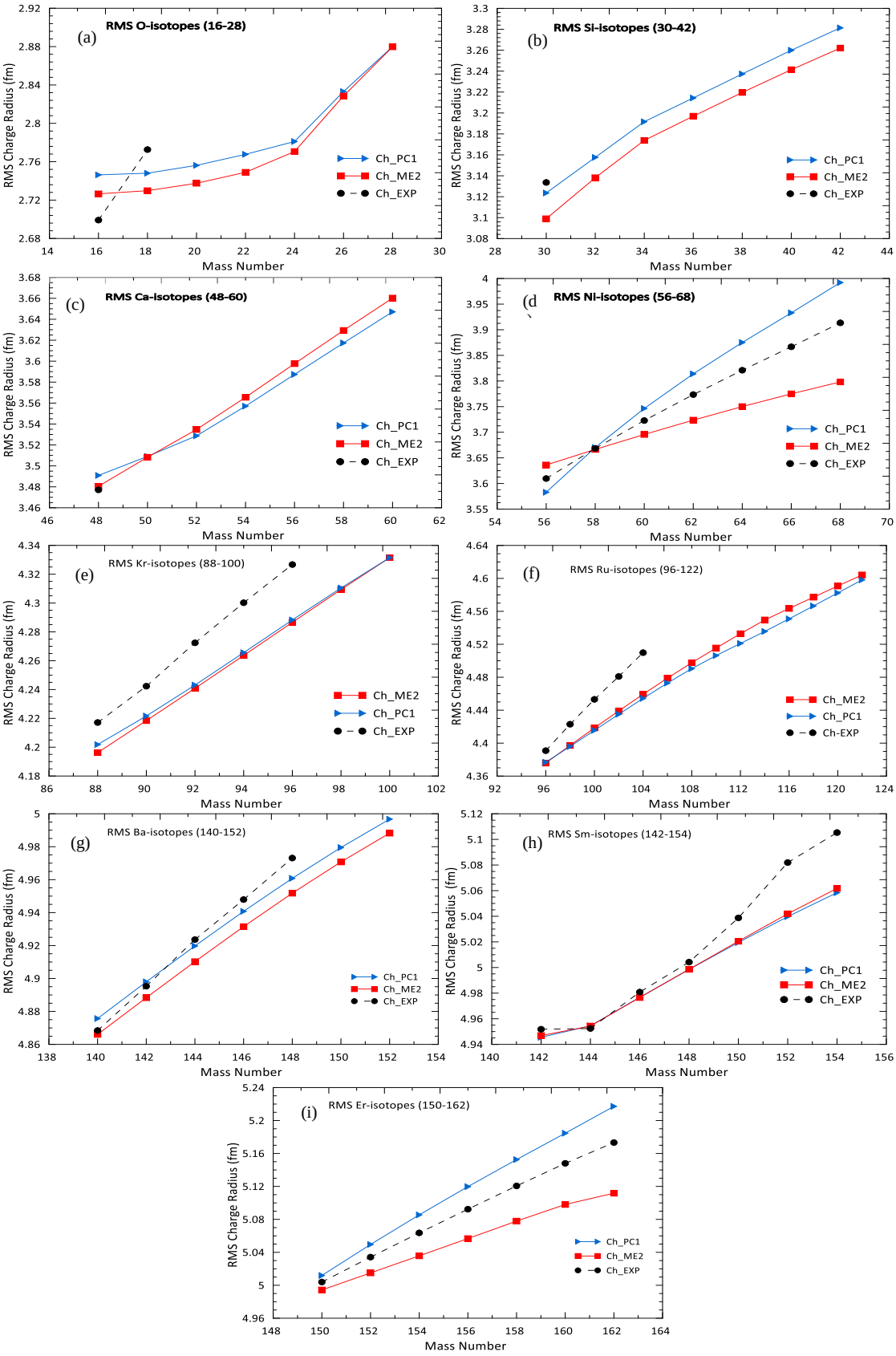

Figure 4: RMS charge radii in fm as a function of mass number (A) for even-even: (a) $^{16-28}$O, (b) $^{30-42}$Si, (c) $^{48-60}$Ca, (d) $^{56-68}$Ni, (e) $^{88-100}$Kr, (f) $^{96-122}$Ru, (g) $^{140-152}$Ba, (h) $^{142-154}$Sm and (i) $^{150-162}$Er isotopes, using ME2, PC1 interactions. In comparison with the experimental data of Angeli and Marinova [26].

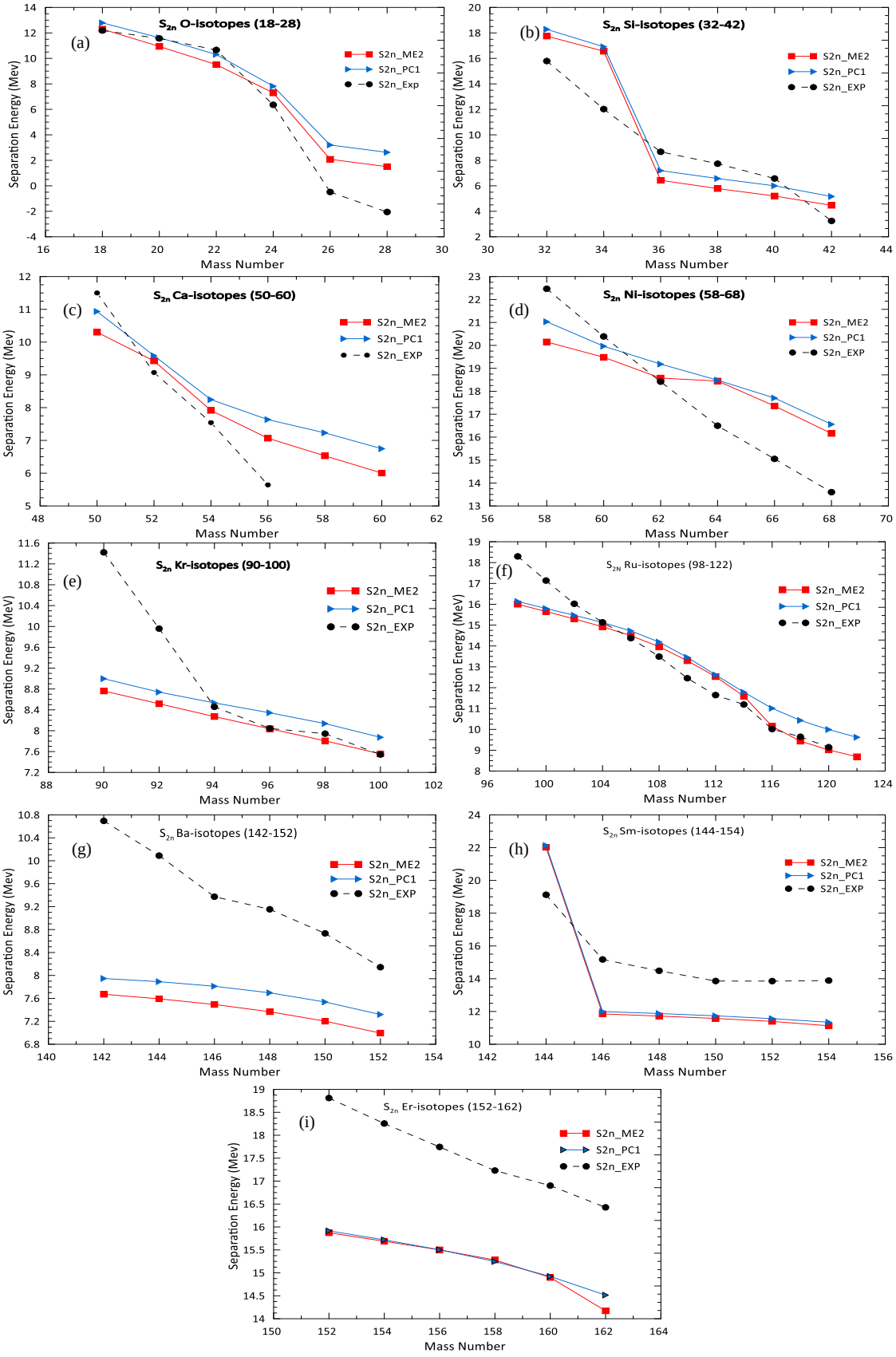

Figure 5: S_{2n} in MeV as a function of mass number (A) even-even (a) $^{16–28}$O, (b) $^{30–42}$Si, (c) $^{48–60}$Ca, (d) $^{56–68}$Ni, (e) $^{88–100}$Kr, (f) $^{96–122}$Ru, (g) $^{140–152}$Ba, (h) $^{142–154}$Sm and (i) $^{150–162}$Er isotopes, using ME2, PC1 interactions. In comparison with the experimental data of the National Nuclear Data Center [25].

The mass density distribution for ^{28}O suggests that it has a compact nucleus with a well-defined spatial arrangement of nucleons. The density profile demonstrated a central peak, which indicates a strong nuclear binding force. By analyzing the contour lines in the figure, it is apparent that ^{28}O has a spherical shape rather than exhibiting triaxial deformation. This spherical shape is a result of the specific nuclear structure and interactions present in this isotope.

The mass density distribution of ^{42}Si indicated a more spread-out nucleus compared to ^{28}O, with a wider distribution of nucleons. Variations in density profiles suggest changes in nuclear structure and neutron-proton interactions. The nuclear shape of ^{42}Si differs from ^{28}O. This nucleus has a magic number of N=28, which requires a strong spin-orbit interaction. The ground state is localized around the oblate-shaped energy minimum at (β, γ) = (0.35, 60◦).

The mass density distribution for ^{68}Ni showed a nucleus with a well-defined central peak and a broader distribution of nucleons compared to ^{60}Ca. Variations in density profiles could indicate changes in nuclear structure and pairing effects. According to the triaxial deformations curves shown in Figs. 6, it can be inferred that ^{68}Ni nuclei, which have a single-shell closure, exhibit a spherical shape with values of $\beta = \gamma = 0$. The mass density distribution for ^{100}Kr indicated a central peak and a broader distribution of nucleons compared to ^{68}Ni. Variations in density profiles could indicate changes in nuclear structure, magic numbers, and shell effects. The contour plot of the ^{100}Kr nucleus showed a sharp transition from a prolate ground state to an oblate one. The occurrence of a triaxial shape transition can be attributed to the competition between different nuclear forces and energy considerations. The mass density distribution for ^{122}Ru exhibited a well-defined central peak and a broader distribution of nucleons. Variations in density profiles could indicate changes in nuclear structure and pairing effects. Triaxial deformation in ^{122}Ru was almost spherical, and a rising hill pushing it towards the right, making it more axial (prolate).

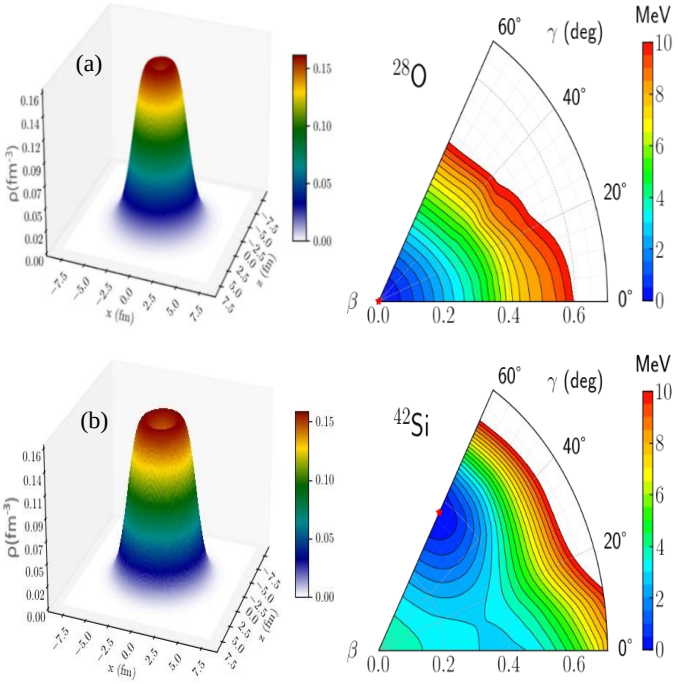

Figure 6: Mass density in fm^{-3} for even-even (a) ^{28}O, (b) ^{42}Si, using PC1 interaction.

The mass density distribution for ^{152}Ba showed a central peak and a broader distribution of nucleons. Variations in density profiles could reflect changes in nuclear structure, magic numbers, and shell closures.^{152}Ba isotopes displayed prolate deformation at their absolute minima. The mass density distribution for ^{154}Sm showed a distinct central peak and a broader distribution of nucleons. The triaxial deformation demonstrated an increase in the depth of both prolate and oblate shapes, as well as the emergence of a pronounced prolate deformation. This deformation is more rigid with respect to the γ degree of freedom. The mass density distribution for ^{162}Er showed a central peak and a broader distribution of nucleons. Variations in density profiles could reflect changes in nuclear structure, magic numbers, and shell closures.

The mass density distribution for ^{60}Ca exhibited a well-defined central peak, indicating a compact nucleus with a high nucleon concentration. Variations in density profiles could reflect the influence of magic numbers and shell closures. The triaxial deformation in ^{60}Ca suggests a symmetric shape.

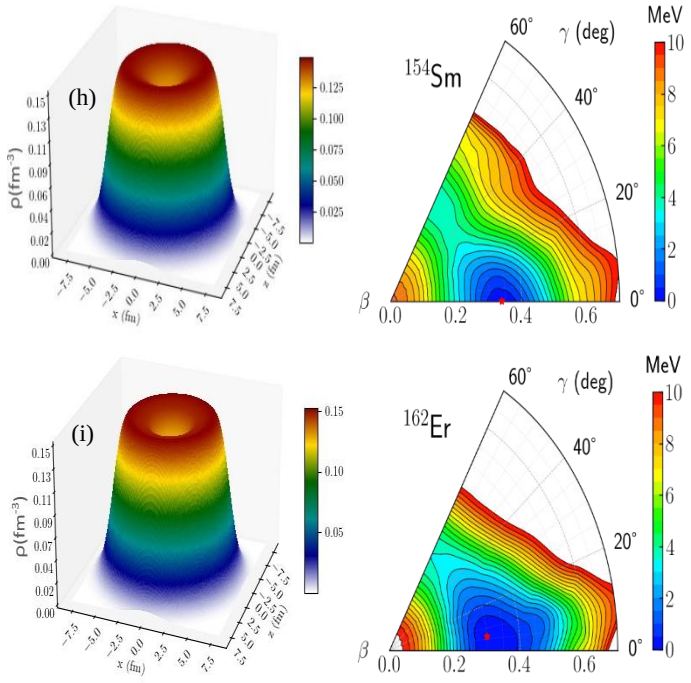

Figure 6 continued but for (h) ^{154}Sm and (i) ^{162}Er.

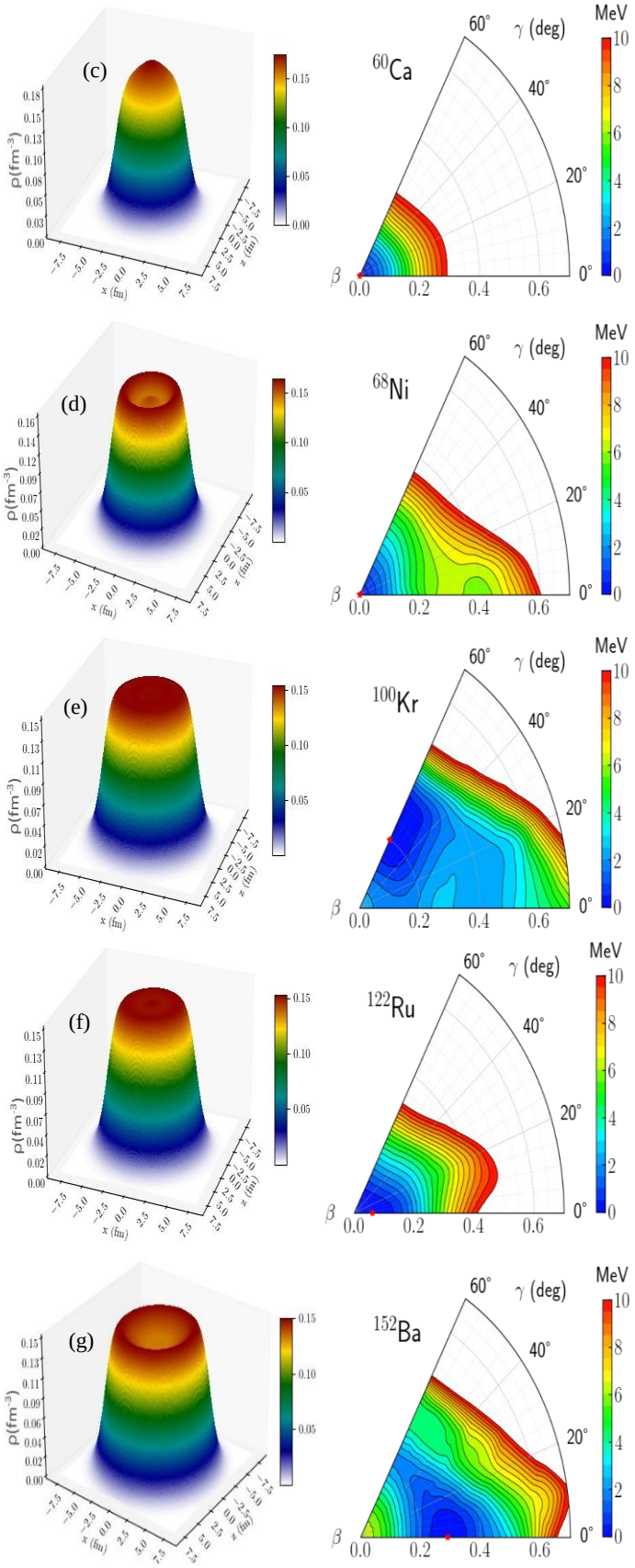

Figure 6 continued but for but for (c) ^{60}Ca, (d) ^{68}Ni, (e) ^{100}Kr, (f) ^{122}Ru, (g) ^{152}Ba.

4. Conclusions

The present study utilized the RHB method with different parameterizations to calculate the ground state nuclear properties of neutron-rich heavy nuclei near the drip line. The RHB demonstrated the effectiveness of approximating highly interacting systems with quasi-particles. This approach allows for the study of complex many-body systems by transforming them into more manageable forms, enabling the calculation of nuclear properties near the drip line. The DD-PC1 and DD-ME2 interactions in the RMF calculations play a crucial role in accurately describing the nuclear properties of neutron-rich nuclei. These interactions capture the nuanced effects of the nuclear environment, leading to improved agreement with experimental data. The comparison of theoretical results with experimental data underscores the predictive power of advanced nuclear physics models in capturing the intricate dynamics of neutron-rich nuclei. The success of the DD-PC1 interaction in reproducing key nuclear properties highlights the importance of selecting appropriate effective interactions for accurate predictions. The observed variations in triaxial deformation across different nuclei, such as prolate, oblate, and spherical shapes, indicate the presence of shape transitions in the nuclear structure. These transitions are influenced by the competition between different nuclear forces and energy considerations, leading to changes in the overall shape of the nucleus.

Conflicts of Interest

The authors declare they have no competing interests.

References

1. G. Gangopadhyay, J. Phys. G Nucl. Par. Phys. **37**, 015108 (2010). DOI: 10.1088/0954-3899/37/1/015108.
2. S. Marcos, R. J. Lombard, and J. Mareš, Phys. Rev. C **57**, 1178 (1998). DOI: 10.1103/PhysRevC.57.1178.
3. J. S. Wang, W. Q. Shen, Z. Y. Zhu, J. Feng, Z. Y. Guo, W. L. Zhan, G. Q. Xiao, X. Z. Cai, D. Q. Fang, H. Y. Zhang, and Y. G. Ma, Nucl. Phys. A **691**, 618 (2001). DOI: 10.1016/S0375-9474(01)00591-7.
4. B. Yaghmaei, A. A. Mehmandoost-Khajeh-Dad, and V. Dehghani, Nucl. Phys. A **1017**, 122353 (2022). DOI: 10.1016/j.nuclphysa.2021.122353.
5. D. S. Golubev and A. D. Zaikin, Phys. Rev. B **62**, 14061 (2000). DOI: 10.1103/PhysRevB.62.14061.
6. J. Suhonen, *From Nucleons to Nucleus: Concepts of Microscopic Nuclear Theory* (Verlag Berlin Heidelberg, Springer Science & Business Media, 2007).
7. H. Flocard, P. Quentin, A. K. Kerman, and D. Vautherin, Nucl. Phys. A **203**, 433 (1973). DOI: 10.1016/0375-9474(73)90357-6.
8. A. A. Alzubadi, Indian Journal of Physics **89**, 619 (2015). DOI: 10.1007/s12648-014-0614-3.
9. G. A. Lalazissis, J. König, and P. Ring, Phys. Rev. C **55**, 540 (1997). DOI: 10.1103/PhysRevC.55.540.
10. M. V. Stoitsov, J. Dobaczewski, W. Nazarewicz, and P. Ring, Comp. Phys. Commun. **167**, 43 (2005). DOI: 10.1016/j.cpc.2005.01.001.
11. A. A. Allami and A. A. Alzubadi, Int. J. Mod. Phys. E **29**, 2050090 (2020). DOI: 10.1142/s0218301320500901.
12. W.-H. Long, N. Van Giai, and J. Meng, Phys. Lett. B **640**, 150 (2006). DOI: 10.1016/j.physletb.2006.07.064.
13. W. H. Long, P. Ring, J. Meng, N. Van Giai, and C. A. Bertulani, Phys. Rev. C **81**, 031302 (2010). DOI: 10.1103/PhysRevC.81.031302.
14. J. Meng, Nucl. Phys. A **635**, 3 (1998). DOI: 10.1016/S0375-9474(98)00178-X.
15. T. Nikšić, D. Vretenar, and P. Ring, Prog. Part. Nucl. Phys. **66**, 519 (2011). DOI: 10.1016/j.ppnp.2011.01.055.
16. M. El Adri and M. Oulne, European Phys. J. Plus **135**, 268 (2020). DOI: 10.1140/epjp/s13360-020-00277-z.

17. T. Nikšić, D. Vretenar, P. Finelli, and P. Ring, Phys. Rev. C **66**, 024306 (2002). DOI: 10.1103/PhysRevC.66.024306.
18. H. Abusara, A. V. Afanasjev, and P. Ring, Phys. Rev. C **85**, 024314 (2012). DOI: 10.1103/PhysRevC.85.024314.
19. C. Fuchs, H. Lenske, and H. H. Wolter, Phys. Rev. C **52**, 3043 (1995). DOI: 10.1103/PhysRevC.52.3043.
20. M. Piarulli and I. Tews, Front. Phys. **7**, 245 (2020). DOI: 10.3389/fphy.2019.00245.
21. S. Typel and H. H. Wolter, Nucl. Phys. A **656**, 331 (1999). DOI: 10.1016/S0375-9474(99)00310-3.
22. V. Kumar, P. Kumar, V. Thakur, S. Thakur, and S. K. Dhiman, Nucl. Phys. A **1022**, 122429 (2022). DOI: 10.1016/j.nuclphysa.2022.122429.
23. T. Mundo and V. De Souza, Boletim. Soci. de Astro. Brasileira **34**, 253 (2023).
24. H. Hergert, Front. Phys. **8**, 1 (2020). DOI: 10.3389/fphy.2020.00379.
25. T. Nikšić, D. Vretenar, and P. Ring, Phys. Rev. C **78**, 034318 (2008). DOI: 10.1103/PhysRevC.78.034318.
26. B. N. Laboratory and N. D. S. International Atomic Energy Agency. *National Nuclear Data Center*; https://www.nndc.bnl.gov/.
27. I. Angeli and K. P. Marinova, Atom. Data Nucl. Data Tables **99**, 69 (2013). DOI: 10.1016/j.adt.2011.12.006.

دراسة التركيب النووي باستخدام طريقة معدل المجال النسبي

سحر ماجد اسماعيل[1] وعلي عبد اللطيف كريم[1]
[1]قسم الفيزياء، كلية العلوم، جامعة بغداد، بغداد، العراق

الخلاصة

تبحث الدراسة الحالية في البنية النوويةلانويه زوجيه –زوجيه مختارة غنية بالنيوترونات و تمتد من خط الاستقرار إلى خط التقاطر النيوتروني باستخدام نهج معدل المجال النسبي. على وجه التحديد، تشمل الانويه التي تمت دراستها $^{16–28}$O, $^{30–42}$Si, $^{48–60}$Ca, $^{56–68}$Ni, $^{88–100}$Kr, $^{96–122}$Ru, $^{140–152}$Ba, $^{142–154}$Sm, and $^{150–162}$Er. تم استخدام طريقة Hartree-Bogoliubov (RHB) النسبية، والتي تتضمن تفاعلات اقتران النقطة الفعالة المعتمدة على الكثافة (DD-PC) وتبادل الميزون المعتمد على الكثافة (DD-ME). تم توضيح تأثير هذه التفاعلات من خلال حساب خصائص البنية النووية المختلفة، بما في ذلك طاقة الربط (BE)، والطاقة الحركية (KE)، وطاقة الاقتران (PE)، وجذر متوسط مربع نصف قطر الشحنة، وطاقة فصل النيوترونات (S_2n)، والكثافة الكتلية (e_m)، والتشوه ثلاثي المحاور. وتمت مقارنة النتائج المحسوبة مع البيانات التجريبية المتاحة. من الواضح أن تقريب RMF، خاصة مع التفاعلات الفعالة DD-ME2 وDD-PC1، أثبت أنه تقريبا جيدا لدراسة الخواص النووية بالقرب من خطوط التقاطر وبعيدًا عن الاستقرار، مما يوفر نظرة ثاقبة لسلوك النوى الغريبة أو الهالة.

الكلمات المفتاحية: نظرية معدل المجال النسبي ، الانوية الغنية بالنيوترونات، تبادل الميزون، نقطة الاقتران, النوى الزوجية-الزوجية.